

# Attenuation Correction in Cardiac SPECT without a Transmission Measurement

Jerold W. Wallis, Tom R. Miller and Paul Koppel

*Mallinckrodt Institute of Radiology, Washington University School of Medicine, St. Louis, Missouri*

The accuracy of SPECT cardiac perfusion imaging is impaired by artifacts induced by nonuniform gamma-ray attenuation. This study proposes a method to estimate attenuation in the chest of patients without the additional hardware and expense of transmission imaging. **Methods:** After the standard  $^{201}\text{Tl}$  or  $^{99\text{m}}\text{Tc}$ -sestamibi delayed images were obtained,  $^{99\text{m}}\text{Tc}$  macroaggregated albumin (MAA) was injected and dual-energy SPECT acquisition was performed with windows centered at 140 keV and 94 keV. Lung contours were obtained by thresholding the on-peak (140 keV) reconstructions. Outer body contours were defined from images produced by reconstruction of the lower energy scatter window obtained simultaneously at the time of the lung (MAA) imaging. Following assignment of standard attenuation values to the lung and nonlung (soft tissue) regions attenuation correction was achieved by means of a modified iterative Chang algorithm. The results were quantitatively evaluated by imaging of a cardiac phantom filled with uniform activity placed in a chest phantom. Sensitivity to the choice of lung and soft tissue attenuation values, the choice of the threshold used for lung segmentation, and errors in registration of the attenuation map were assessed. **Results:** Application of this technique in a chest phantom and in patients imaged with both  $^{201}\text{Tl}$  and  $^{99\text{m}}\text{Tc}$ -sestamibi resulted in improvement in artifactually decreased inferior wall activity without adversely affecting the other walls. The results were relatively insensitive to choice of values for lung and soft-tissue attenuation, lung thresholding, and small ( $\leq 1.3$  cm) registration errors. **Conclusion:** This simple method corrects for nonuniform attenuation in males; studies are underway to adapt the method to determine breast contour in females and to determine the value of the method in clinical practice.

**Key Words:** SPECT; attenuation correction; cardiac perfusion imaging; coronary artery disease

**J Nucl Med 1995; 36:506–512**

**C**ardiac perfusion imaging using SPECT is useful in the diagnosis of coronary artery disease. However, study quality is impaired by significant artifacts induced by nonuniform gamma-ray attenuation in the chest. This can result in apparently decreased uptake in the inferior wall (due to

diaphragm attenuation) and the anterior wall (due to attenuation from breast tissue) (1,2); such artifacts can lead to incorrect interpretation in these regions, particularly since the degree and exact location of attenuation artifacts can vary between individuals.

Several methods have been proposed to correct for these artifacts by measuring attenuation in the chest with a transmission source (3–7), but these methods require expensive additional hardware and can require significant additional imaging time. This paper proposes a method to estimate attenuation in the chest which does not require additional hardware and adds only minimal imaging time. The lung regions are defined with use of an injection of  $^{99\text{m}}\text{Tc}$ -MAA and body outlines are obtained from off-peak images.

## METHODS

### Cardiac Emission Data

An elliptical phantom with lung and cardiac inserts (Data Spectrum Corp., Chapel Hill, NC) was employed for the phantom experiments. The lung inserts were filled with damp Styrofoam beads, the heart was filled with a solution containing 0.5 mCi  $^{99\text{m}}\text{Tc}$  pertechnetate and the rest of the phantom was filled with water to represent soft tissue. To emphasize the effect of diaphragm attenuation, the cardiac insert was fastened approximately 1.5 cm below its standard position, placing the inferior myocardial wall below the lower lung boundary. Imaging was performed in 64 positions over  $180^\circ$  from  $45^\circ$  right-anterior-oblique to  $45^\circ$  left-posterior-oblique using a rotating gamma camera (Multi-SPECT, Siemens Medical Systems, Hoffman Estates, IL), with a total acquisition time of 10 min. To simulate a typical  $180^\circ$  cardiac acquisition, the extra projection images from this triple-headed gamma camera were not utilized in the reconstruction. The projections were reconstructed using rampfiltered backprojection; high frequency noise was decreased with use of post-reconstruction three-dimensional Wiener filtering (8).

Patient cardiac images were obtained using our standard clinical protocols on the same rotating gamma camera using a 20% window centered about either 70 keV ( $^{201}\text{Tl}$ ) or 140 keV ( $^{99\text{m}}\text{Tc}$ ). Patients were injected during treadmill stress or dipyridimole infusion with either 3.0 mCi  $^{201}\text{Tl}$  or 7.0 mCi  $^{99\text{m}}\text{Tc}$  sestamibi; images were acquired following stress and again after a 3–4 hr delay. Patients who were studied using  $^{99\text{m}}\text{Tc}$ -sestamibi were re-injected with a 25 mCi dose before the delayed images were obtained. Reconstructions were performed as described above using  $180$  degrees of projection data.

Received Jan. 14, 1994; revision accepted Aug. 22, 1994.

For correspondence or reprints contact: Jerold W. Wallis, M.D., Mallinckrodt Institute of Radiology, 510 South Kingshighway, St. Louis, MO 63110.

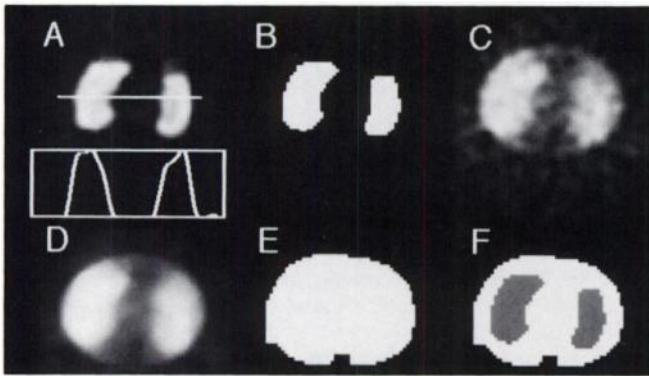


**FIGURE 1.** The steps in the generation of the attenuation map, shown for a single slice in the cardiac region of the chest phantom. The Weiner filtered on-peak transaxial slices of the lungs (A) are thresholded to form a binary image (B); a line profile through the lungs is also shown. The off-peak transaxial slices are reconstructed using a relatively smooth Butterworth filter (C) and then a median filter is applied (D). This image is thresholded to form a binary image (E), which is combined with the earlier lung outlines to yield the final attenuation map (F).

### Determination of Attenuation Map

The chest attenuation map consists primarily of regions of soft tissue (water) density and regions of lung. The spine does not interfere with imaging in a typical 180° cardiac acquisition, and the remaining bones of the thorax are relatively thin; they are not distinguishable from water density on transmission images obtained using a gamma-camera flood source (4). Thus, an estimated attenuation map can be created from knowledge of the outer body contour, lung boundaries and approximate attenuation coefficients for lung and water. The steps in the generation of the attenuation map are shown in Figure 1.

**Lung Boundaries.** The lung contours were obtained after injection of <sup>99m</sup>Tc-MAA (Fig. 1A, B). To determine the margins of the lungs in the phantom study, the Styrofoam was removed after the emission data were obtained, and the lung cavities were filled with a solution containing 2 mCi of <sup>99m</sup>Tc pertechnetate. The phantom was then replaced under the gamma camera in a position identical to that used for the emission imaging. Lung boundaries in patient studies were obtained by injection of 4.0 mCi <sup>99m</sup>Tc-MAA after completion of the delayed <sup>201</sup>Tl or <sup>99m</sup>Tc-sestamibi images. Care was taken to avoid patient motion between the delayed cardiac images and the lung images. Projection data were obtained over 360° using 90° angles, with a total acquisition time of 6 min. A 20% window centered at 140 keV was used for the lung acquisition; simultaneous acquisition of a lower energy window was also performed to obtain the outer body contour, as described below.

The first step in data analysis was reconstruction of the transaxial lung emission images, using the same techniques as employed for the cardiac emission data. Segmentation of the resulting images to extract the lung boundaries was performed using a threshold of 35% of peak lung activity followed by a three-dimensional dilation/erosion operation (9). After thresholding to produce a starting mask, a dilation (which increases the region size by one pixel in all directions) was performed to eliminate any small holes in the lung regions, followed by an erosion (decreasing the region size by one pixel) to preserve the original geometry. A relatively low threshold was chosen to permit areas of hypoperfused lung to be correctly classified. This operation was confirmed

to yield lungs of the appropriate size by processing of a cylindrical phantom of known dimensions.

In patients studied with <sup>99m</sup>Tc-sestamibi, the heart was visible on the <sup>99m</sup>Tc-MAA images. In order to remove the myocardium from these images, the sestamibi images obtained before MAA injection were subtracted from the <sup>99m</sup>Tc-MAA images before determination of the lung boundaries. The proportion of sestamibi images subtracted was chosen visually to substantially eliminate counts in the region of the myocardium on the resulting images. Processing lung data from the phantom study differed slightly from processing of patient lung data in one respect—there was significantly greater attenuation of the phantom's water-filled lungs during the lung emission imaging, a first-order Chang correction (10) was applied to the reconstructed lung data. The alternative of adding radioactivity to Styrofoam beads in the lung cavity was not chosen because of the difficulty in achieving a uniform distribution of tracer.

**Outer Body Boundaries.** Outer body contours were defined from images produced by reconstruction of a lower energy scatter window obtained simultaneously at the time of the lung (MAA) imaging (Fig. 1C-E). A 30% window centered at 94 keV was empirically chosen to yield the best definition of the body contour. Ramp-reconstructed images were smoothed using a three-dimensional Butterworth filter (order 5, cutoff 0.225/pixel) with subsequent three-dimensional 5 × 5 × 5 median filtering. These filtering operations were accelerated using three-dimensional versions of the methods of McClellan (8,11) and Huang (12), respectively. A small background region exterior to the body on all slices was then chosen manually to serve as a count reference. A threshold was then chosen interactively to differentiate the degree of activity exterior to the body from that within the body; a value of 1.4–1.7 × the mean value in this background region on each individual slice was found to optimally distinguish the body boundary. The body region was then automatically defined by the computer on all slices. This use of a reference region allowed the actual threshold value to vary across slices; such variation was found to be necessary because the source distribution from which scattered counts were emanating was not constant. Other edge detection techniques could likely be employed with similar results. Validation of outer body detection was performed by processing of the chest phantom with comparison to the known elliptical dimensions of the phantom.

**Attenuation Coefficients.** For technetium-energy myocardial studies, the broad-beam attenuation coefficient for water (0.13 cm<sup>-1</sup>) was assigned to the regions designated to be soft tissue, represented by all the volume within the outer body contour not in the lungs. A value of .047 cm<sup>-1</sup> was used for the lungs based on published estimates (6,13) and a value of .07 cm<sup>-1</sup> was used for the damp Styrofoam. When thallium was used as the perfusion agent, these values were increased by 20% based on the ratio of the narrow-beam attenuation coefficients in water for the 68–83 keV Hg x-rays from <sup>201</sup>Tl and the 140 keV gamma-ray from <sup>99m</sup>Tc (14). The final attenuation map is shown in Figure 1F.

### Reconstruction and Processing

Attenuation correction was achieved by use of an iterative reconstruction algorithm. A modified version of the iterative Chang algorithm (10) was employed which allowed for variable attenuation, with the attenuation map utilized in the projection step of the iterative reconstruction. The depth-dependent three-dimensional point spread function was not modeled in the projection step because of the increased computational complexity. Five

iterations were found to be sufficient for attenuation correction. Following reconstruction, standard SPECT cardiac processing was performed, leading to images in the short, vertical long-, and horizontal long-axis planes and a bullseye display (15). When the same study was processed under varying conditions of attenuation correction, identical cardiac rotation angles and bullseye sampling was performed.

### Error Sensitivity

**Misregistration Error.** To determine the effect of misregistration errors between the attenuation map and the emission data, reconstructions of the chest phantom containing a plastic heart filled with uniform activity were performed following shifting of the attenuation map by 2, 4 and 6 pixels, corresponding to 1.34, 2.68 and 4.02 cm, respectively in the x (lateral), y (antero-posterior) and z (cranio-caudal) directions. In addition to visual assessment of the mis-registered reconstructions, the uniformity of activity in the reconstructed myocardium was quantified by creation of a bullseye plot and determination of the relative s.d. (s.d./mean counts) of the bullseye counts. For this quantitative analysis the entire bullseye was analyzed with the exception of the extreme basal portion of the bullseye (the edge of the myocardium). The ratio of activity in the anterior and inferior wall (omitting the peri-apical region of the inferior wall) was also computed; this will be referred to as the anterior/posterior ratio.

**Lung Thresholding Error Sensitivity.** The same chest and heart phantom was used to assess the effect of different threshold values for determination of lung boundaries. Choice of different thresholds resulted in slightly different lung sizes in the attenuation map. Reconstructions were performed with threshold values of 25%, 35% and 45% of peak lung activity. Following reconstructions with each of the attenuation maps, bullseye displays were generated and the uniformity of activity in the myocardium was assessed as described above.

**Sensitivity to Error in Assigned Attenuation Coefficients.** Although the attenuation coefficient of the lungs will vary slightly from one individual to another (6), a single estimated value is employed in this technique. To assess the sensitivity to choice of attenuation value, the lung attenuation coefficient was varied in reconstructions of the chest phantom over a range from 0.0 to 0.13  $\text{cm}^{-1}$ , with assessment of the effect on the reconstructed cardiac images as described earlier. The effect of variation of the soft-tissue attenuation coefficient was also assessed, with reconstructions employing values from 0.09  $\text{cm}^{-1}$  to 0.17  $\text{cm}^{-1}$ .

## RESULTS

### Phantom Studies

**Contour Validation.** The attenuation map following extraction of the lung and outer body contours and combination of these regions is shown in Figure 2 (top) for the phantom study. The major and minor axes of the elliptical outer body contour were computed from the segmented images to be 30.8 cm and 22.1 cm, respectively; these compared to measurements of 31.5 cm and 23.5 cm in the actual phantom. To evaluate the lung contours, the segmented image was compared to a transmission image of the phantom (obtained from a separate PET scan), shown in Figure 2 (bottom). As can be seen in the figure, the lung outlines are similar to those derived from the transmission study. The increased attenuation from the plastic spine resulted in a posterior indentation in the estimated outer

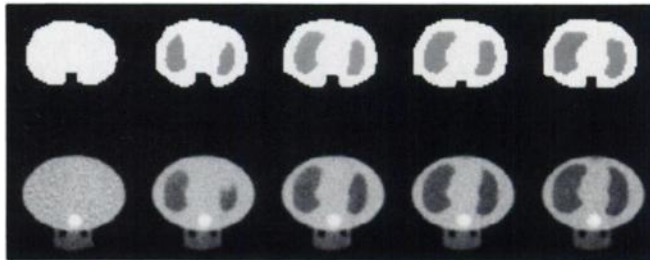


**FIGURE 2.** Following processing of the body phantom as described above, the estimated attenuation map is shown at multiple levels (top); for comparison, PET transmission images are also shown (bottom) at approximately the same levels. Slight irregularities in the automatically detected contour due to the spine and in the right chest wall (viewer's left) could be corrected either automatically or with operator intervention, but would not be significant for a typical 180° acquisition.

body contour, evident in Figure 2. This did not affect the reconstruction as it was not within the projection path of the 180° emission data; if 360° acquisition were being employed, a structure of bone density could be automatically placed in the midline posterior body to represent the spine. The automatically determined body contours in the limited patient studies corresponded well with expected body outlines and with visually evident boundaries on the scatter images.

**Cardiac Reconstruction.** Figure 3 shows bullseye plots of the cardiac phantom containing uniform activity imaged in the chest phantom. The clinical reconstruction (without attenuation correction) and the attenuation corrected reconstruction are shown. The apparently decreased uptake in the inferior wall (due to diaphragm attenuation) is not present after attenuation correction. Quantitative analysis showed that the ratio of the mean counts in the anterior and posterior regions of the bullseye image improved from 1.17 without attenuation correction to 1.02 following correction. The uniformity of the myocardium as measured by the relative s.d. of the counts in the bullseye plot improved from 13.7% without attenuation correction to 8.6% with correction, corresponding to the visually more uniform activity evident in the corrected image in Figure 3.

**Sensitivity Analysis.** Figure 4 shows the effect of increasing offsets of the attenuation map on the reconstructed heart. It can be seen that a misregistration error of 4 cm can result in artifactual nonuniformity in the myocardium of a degree approaching that seen without attenuation correction. Visually and quantitatively there was minimal change in uniformity of the myocardium when a 1.3 cm registration error was present, while a 2.7 cm registration error resulted in mild but definite nonuniformity in the appearance of the bullseye. These findings are in approximate agreement with data from PET imaging, where a 2 cm misalignment was judged to result in significant cardiac artifacts (16). Note, however, that the chest phantom employed had a 1.5 cm region of soft-tissue density between the heart and the lungs, as might be seen in an obese person with pericardial or epicardial fat. The requirements for alignment are likely

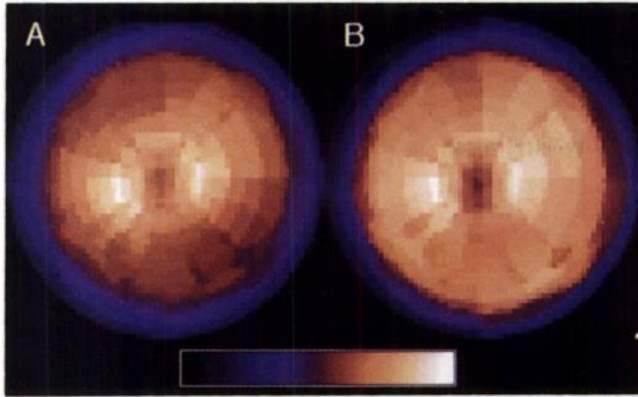


**FIGURE 3.** Comparison of bullseye plots of the uniform cardiac phantom imaged in the chest phantom, with reconstruction both without (A) and with (B) attenuation correction.

to be slightly more demanding in a thin patient, in which a 1.3 cm shift would move the heart substantially into the lung region.

It can be seen in Figure 4A that a  $-1.3$ -cm shift in the y direction actually improved cardiac uniformity slightly. While it is conceivable that this represents a registration error, resulting from repositioning of the phantom after filling the lungs with activity during our experiment, it is more likely that a slight offset in one of the six directions happened by chance to slightly improve the nonuniformity arising from other sources (e.g., partial volume effect, depth-dependent resolution). It can be seen in Figure 4B that the anterior/posterior ratio is most accurate when there is no z-axis shift, appropriately placing the inferior wall in the abdomen and the anterior wall in the chest density portions of the phantom; significant movement either in the cranial or caudal directions places these two walls in the same attenuation region, lessening the effect of the correction. Motion in the x and y directions slightly increased or decreased the effect of the correction by placing the heart closer or further from the chest wall.

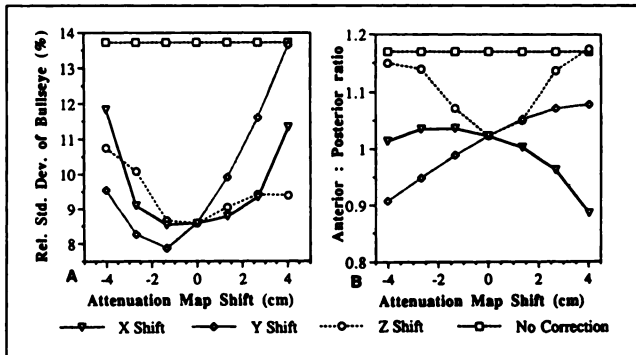


**FIGURE 4.** The effect of misregistration of the attenuation map in the x, y and z directions upon (A) the uniformity of the reconstructed myocardium as assessed by the standard deviation of the pixels in the bullseye (see text) and (B) the anterior : posterior ratio. The uniform cardiac phantom was imaged in the chest phantom. For reference, the values corresponding to the uncorrected myocardial reconstructions are also shown.

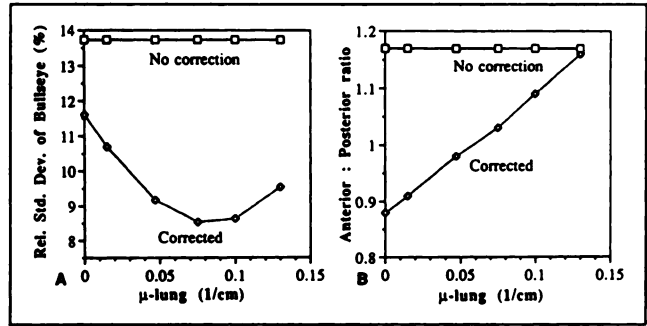


**FIGURE 5.** Graphs depicting the effect of varying the lung attenuation coefficient upon the reconstructed myocardium in the uniform cardiac phantom imaged in the chest phantom. (A) and (B) are as in Figure 4.

The results following utilization of different lung attenuation coefficients are shown in Figure 5. While use of extreme values such as those corresponding to water or air results in significant nonuniformity of the cardiac bullseye, this data suggests that variation within two s.d. of an average lung attenuation value ( $0.045 \text{ cm}^{-1}$  s.d.  $.013$ ) (13) would still result in substantial improvement in myocardial uniformity. The effect of choice of different lung thresholds was assessed; the relatively sharp lung boundaries, as evident in Figure 1A resulted in only minimal change in lung boundary position. Utilizing a value of 25% or 45% for the threshold rather than our standard value of 35% resulted in only a 3 mm shift in lung boundary positions, and had no significant effect on the bullseye uniformity or anterior/posterior ratio. The effect of variation in the soft-tissue attenuation coefficient is presented in Figure 6. Minor changes in the effective soft-tissue attenuation might be encountered due to varying degrees of scatter in obese patients. Errors of 10% in the soft-tissue attenuation coefficient had minimal effect on the myocardium, and errors of 30% still resulted in more accurate reconstructions than those obtained without attenuation correction.

#### Patient Studies

Figures 7 and 8 illustrate the estimated attenuation maps and the reconstructed clinical images both with and without attenuation correction in two patients, one imaged with

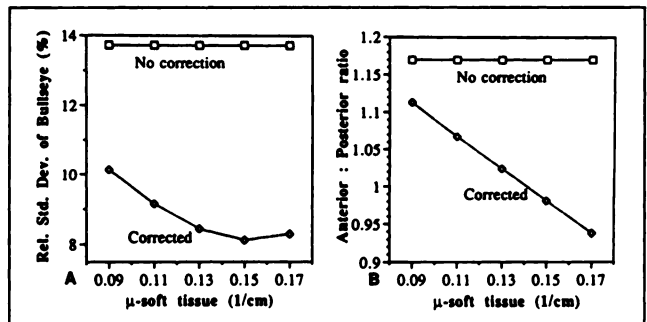


**FIGURE 6.** The effect of variation in the soft-tissue attenuation coefficient upon the reconstructed myocardium. (A) and (B) are as in Figure 4.

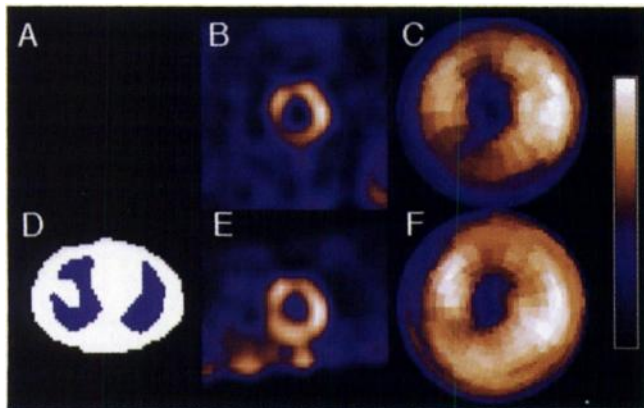


**FIGURE 7.** Images from a cardiac study employing  $^{201}\text{Tl}$  in a patient with a large anteroseptal and apical infarction. (A) attenuation map used in clinical reconstruction (i.e. none). (B and C) Mid-cardiac short-axis slice and bullseye plot without attenuation correction, showing inferior attenuation artifact as well as the apical infarct (D) attenuation map from a mid-cardiac transaxial slice, showing body outline and lungs; the dome of the right hemi-diaphragm is evident at this level. (E and F) Mid-cardiac short-axis slice and bullseye plot following attenuation correction.

$^{201}\text{Tl}$  (Fig. 7) and one with  $^{99\text{m}}\text{Tc}$ -sestamibi (Fig. 8). The first patient had a large anteroseptal and apical myocardial infarction with extensive disease in the left anterior descending coronary artery. There was no evidence by ECG or catheterization of coronary disease in the inferior wall. The second patient underwent a submaximal treadmill study for evaluation of syncope. In this patient with a low clinical suspicion of coronary disease, a mild reversible septal defect on the stress images was felt to be due to exercise-induced left bundle branch block, and the fixed inferior defect was attributed to diaphragm attenuation. Note the improved appearance of the inferior and inferoseptal walls following attenuation correction in both of these patients with no evidence of coronary artery disease in this region. The areas of known abnormalities were not affected by the attenuation correction.

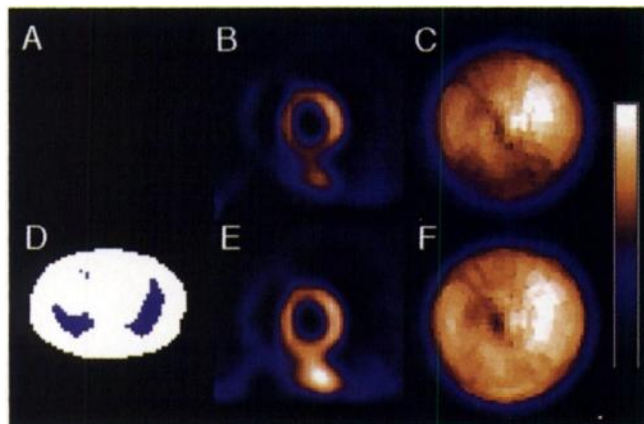


**FIGURE 8.** Images from a cardiac study employing  $^{99\text{m}}\text{Tc}$  sestamibi, in a patient with low clinical suspicion of coronary artery disease, no previous history of infarction, and a mild fixed inferior wall defect consistent with diaphragm attenuation. Image format as in Figure 7.

## DISCUSSION

### Importance of Attenuation Correction

Attenuation effects hinder interpretation of both planar and tomographic myocardial perfusion studies. Attenuation by the diaphragm results in significant inferior wall artifacts in planar perfusion imaging, leading to the clinical practice of right lateral decubitus imaging for the steep oblique view (17,18). Attenuation due to the diaphragm is also present in SPECT imaging performed in the supine position (2), and can result in erroneous interpretation of decreased activity in the inferior wall. The degree of attenuation effect can vary from one individual to another, making it difficult to ascribe a fixed inferior wall defect to attenuation or to infarction in a particular patient. Alternative approaches, such as prone imaging (19,20), have been proposed to partially alleviate this problem, but such methods can lead to anterior wall artifacts and have not become popular in clinical practice.

Similarly, attenuation from breast tissue is a problem both in planar (21,22) and SPECT (2,23) imaging of women. In planar imaging the breast contours are frequently visualized, allowing correction for the effect of attenuation during image interpretation. While the abnormalities in SPECT reconstructions are predominantly in the anterior region, it is often difficult to determine if a particular abnormality is due to attenuation artifact or to coronary disease.

### Methods of Attenuation Correction

Several methods have been proposed for attenuation correction in SPECT. These methods involve determination of the distribution of attenuation coefficients in the chest (the attenuation map). The attenuation coefficients have most frequently been determined by a transmission measurement. Focused collimators with point or lines sources, parallel collimators with flood or moving line sources and an uncollimated gamma camera with a point source have all been used (3-7). While these methods are generally effective, there are associated difficulties such as: the mechanical apparatus can be awkward and expensive; use of focused collimators may result in truncation artifacts; use of different energies for transmission and emission data can result in incorrect attenuation values; and scatter from simultaneous presence of both the emission and transmission sources can degrade the reconstructions.

Other methods, including the one proposed here, estimate rather than measure the attenuation map. Data from computed tomography (CT) have been used for this purpose (24), with registration of the transmission data with the SPECT emission study prior to attenuation correction. A recent paper (25) also proposed using lung perfusion imaging for definition of lung outlines, with use of a radioactive elastic bandage to mark the outer body contour. Other methods to define a convex outer body contour from projection data have also been developed (26-28). Assignment of noise-free attenuation coefficients to segmented transmission images has been proposed in both SPECT

(29) and PET (30,31) to decrease noise propagation from the transmission to the emission reconstructions.

All of these methods employ an iterative reconstruction algorithm to correct for the variable attenuation, since the commonly used first-order Chang correction (10) is only approximate, and its accuracy diminishes in the setting of nonuniform attenuation. In our experience, both iterative likelihood-based techniques employing the expectation maximization algorithm (32,33) and techniques using iterative filtered backprojection (34) result in adequate compensation for attenuation after 5–10 iterations. While it is possible to model the point-spread function during iterative reconstruction to improve image resolution, as has been done both by us (34,35) and others (36–38), this was not done in this investigation to decrease the computational requirements.

#### Comparison of This Method to Use of a Transmission Source

The principal advantages of this method of attenuation correction lie in two areas: (a) simplicity and cost and (b) image quality. The method is indeed simple, requiring only 5–10 min of additional camera time (without manipulation of apparatus such as collimators or flood sources) and semiautomatic additional image analysis. The cost of this approach is negligible, consisting only of the expense of a 4 mCi dose of  $^{99m}\text{Tc}$ -MAA and camera time. These factors are in contrast to the effort and expense associated with specialized collimators and flood sources required for transmission measurement. The added patient radiation dose is only 7%–11% of the  $^{201}\text{Tl}$  or Tc-sestamibi dose.

Issues of image quality are more complex. The method presented here could be criticized as being approximate and inexact, especially in comparison to measurement with transmission sources. The tradeoffs between the two methods may not favor the transmission approach. While the accuracy of the method described here may be less than that of transmission measurement, our sensitivity analysis indicates that anticipated errors in the value of the attenuation coefficients due to normal patient variation will only weakly affect the results. In both this method and when utilizing transmission measurements, care must be taken to keep the emission data and attenuation map aligned. The transmission measurement may lead to loss of contrast in the emission data due to scattered counts when the flood source is imaged simultaneously with the emission data. Conversely, the emission gamma rays may interfere with the transmission measurement. The method proposed here has no such contrast loss or transmission interference because the  $^{99m}\text{Tc}$ -MAA is injected only after the emission data are obtained. Furthermore, a noisy transmission measurement will propagate noise into the reconstruction of the emission data. The method proposed here involves no noise propagation, although there may be a slight offset or bias of counts from the true value. Thus, compared to the method presented here, the transmission technique may yield slightly more accurate attenuation correction, but in

**TABLE 1**  
Imaging Protocols for Estimated Attenuation Correction

Protocol 1	Protocol 2
Standard initial imaging	Standard initial imaging
	Injection of low dose $^{99m}\text{Tc}$ -MAA
	Dual-energy imaging
Standard delayed imaging	Standard delayed imaging
Injection of $^{99m}\text{Tc}$ -MAA	Injection of higher dose $^{99m}\text{Tc}$ -MAA
Dual-energy imaging	Dual-energy imaging

exchange for reduced image contrast and increased noise. Further studies will be required to determine which method yields better clinical results.

#### Imaging in Patients with Lung Disease

Generation of the body outlines by use of scatter from the lungs following  $^{99m}\text{Tc}$ -MAA injection was found to be accurate in men where the scatter source is close to the chest wall. However, in women the breast margin may be significantly farther from the lungs than is the chest wall in men and the body margin is not convex, thus making this margin difficult to distinguish on scatter images. It may be necessary to utilize other methods to create an accurate attenuation map in women. A radioactive binder, such as that proposed by Madsen (25), would reliably delineate the anterior chest wall, but still would not accurately portray concave portions of the body outline. Alternatively, a scattering source outside the body, such as a string marker placed along the sternum, would augment the scatter from the lung activity. Further work in this area is ongoing.

The method assumes that the distribution of lung perfusion adequately reflects the air-filled portions of the lung; this may not be the case in patients with chronic obstructive lung disease who may have nonperfused, air-filled lung regions. To minimize the effect of heterogeneous perfusion, a relatively low threshold was utilized for lung segmentation (so that areas of moderately hypoperfused lung would still be segmented as lung), and a sequence of dilation/erosion steps was employed in the segmentation process to fill in any remaining small defects in the segmented lung region.

#### Imaging Protocols

We envision two possible imaging protocols. Concern over loss of image contrast from scattered lung counts has led us to inject the  $^{99m}\text{Tc}$ -MAA only after all emission data were obtained (Table 1, Protocol 1). There is no loss of contrast due to scattered counts from the  $^{99m}\text{Tc}$ -MAA because the  $^{99m}\text{Tc}$ -MAA is injected only after all emission data have been collected. The disadvantage of this approach—that the first set of images are not corrected for attenuation—may not be a critical issue. For example, if a fixed defect is seen in the inferior wall that disappears after attenuation correction of the second set of images, the defect is likely a diaphragm artifact. Otherwise, the defect likely is due to coronary disease.

The second protocol (Table 1, Protocol 2) yields atten-

uation maps for both sets of perfusion images and should work well when a one-day Tc-sestamibi study is performed. Following the first low dose of sestamibi (e.g. 7 mCi), 1.5 mCi  $^{99m}\text{Tc}$ -MAA is injected and an attenuation map is created. The second dose of sestamibi will typically be much larger (e.g. 25 mCi), thus overwhelming the scatter from the partly-decayed first MAA dose. Finally, a second 2.5 mCi  $^{99m}\text{Tc}$ -MAA injection is made to produce the second attenuation map. Our concern with scatter in a  $^{201}\text{Tl}$  study may be excessive (25); it is possible that Protocol 2 (Table 1) will yield acceptable results with  $^{201}\text{Tl}$ , and further study is warranted. Reduction of the first  $^{99m}\text{Tc}$ -MAA dose to 1–2 mCi may yield acceptable lung boundaries while leading to a barely-detectable loss of contrast in the delayed  $^{201}\text{Tl}$  emission images following a 3–4 hr decay interval.

## CONCLUSIONS

In summary, a method is described that yields attenuation maps for use in correction of myocardial images. This simple, inexpensive method contrasts with most reported techniques that involve expensive and potentially cumbersome transmission measurements. While the anatomic accuracy of the method described here may be slightly inferior to that achieved with the transmission approach, results presented here show good correction for nonuniform attenuation and compare favorably with published reports employing the more complex technique while offering potential advantages of superior image contrast and lower noise. Studies are underway to determine the value of this method in clinical practice.

## ACKNOWLEDGMENT

This work was supported in part by a grant from Siemens Medical Systems, Hoffman Estates, IL.

## REFERENCES

- Manglos SH, Thomas FD, Gagne GM, Hellwig BJ. Phantom study of breast tissue attenuation in myocardial imaging. *J Nucl Med* 1993;34:992–996.
- DePuey EG, Garcia EV. Optimal specificity of thallium-201 SPECT through recognition of imaging artifacts. *J Nucl Med* 1989;30:441–449.
- Manglos SH, Bassano DA, Thomas FD. Cone-beam transmission computed tomography for nonuniform attenuation compensation of SPECT images. *J Nucl Med* 1991;32:1813–1820.
- Tsui BMW, Gullberg GT, Edgerton ER, Ballard JG, Perry JR, McCartney WH, Berg J. Correction of nonuniform attenuation in cardiac SPECT imaging. *J Nucl Med* 1989;30:497–507.
- Frey EC, Tsui BM, Perry JR. Simultaneous acquisition of emission and transmission data for improved thallium-201 cardiac SPECT imaging using a technetium-99m transmission source. *J Nucl Med* 1992;33:2238–2245.
- Manglos SH, Bassano DA, Thomas FD, Grossman ZD. Imaging of the human torso using cone-beam transmission CT implemented on a rotating gamma camera. *J Nucl Med* 1992;33:150–156.
- Tung CH, Gullberg GT, Zeng GL, Christian PE, Datz FL, Morgan HT. Nonuniform attenuation correction using simultaneous transmission and emission converging tomography. *IEEE Trans Nucl Sci* 1992;39:1134–1143.
- Miller TR, Wallis JW, Wilson AD. Interactive reconstruction in single-photon tomography. *Eur J Nucl Med* 1989;15:189–193.
- Serra J. *Image analysis and mathematical morphology*. New York: Academic Press; 1982.
- Chang LT. A method for attenuation correction in radionuclide computed tomography. *IEEE Trans Nucl Sci* 1978;NS-26:638–643.
- McClellan JH, Chan DSK. A two-dimensional FIR filter structure derived from the Chebyshev recursion. *IEEE Trans Circuits Systems* 1977;7:372–378.
- Huang TS, Yang GJ, Yang GY. A fast two-dimensional median filtering algorithm. *IEEE Trans Acoust Speech and Sig Proc* 1979;ASSP-27:13–18.
- Rowell NP, Glaholm J, Flower MA, Cronin B, McCready VR. Anatomically derived attenuation coefficients for use in quantitative single photon emission tomography studies of the thorax. *Eur J Nucl Med* 1992;19:36–40.
- Sorenson JA, Phelps ME. *Physics in nuclear medicine, second edition*. Orlando: Grune and Stratton, Inc.; 1987:Appendix D.
- Miller TR, Starren JB, Grothe RA. Three-dimensional display of positron emission tomography of the heart. *J Nucl Med* 1988;29:530–537.
- McCord ME, Bacharach SL, Bonow RO, Dilsizian V, Cuocolo A, Freedman N. Misalignment between PET transmission and emission scans: its effect on myocardial imaging. *J Nucl Med* 1992;33:1209–1214.
- Johnstone DE, Wackers FJT, Berger HJ, et al. Effect of patient positioning on left lateral thallium-201 myocardial scans. *J Nucl Med* 1979;20:183.
- Gordon DG, Pfisterer M, Williams R, et al. The effect of diaphragmatic attenuation on  $^{201}\text{Tl}$  images. *Clin Nucl Med* 1979;4:150.
- Kiat H, Van TK, Friedman JD, et al. Quantitative stress-redistribution thallium-201 SPECT using prone imaging: methodologic development and validation. *J Nucl Med* 1992;33:1509–1515.
- Segall GM, Davis MJ. Prone versus supine thallium myocardial SPECT: a method to decrease artifactual inferior wall defects. *J Nucl Med* 1989;30:548–555.
- Goodgold HM, Rehder JG, Samuels LD, Chaitman BR. Improved interpretation of exercise  $^{201}\text{Tl}$  myocardial perfusion scintigraphy in women: characterization of breast attenuation artifacts. *Radiology* 1987;165:361–366.
- Stolzenberg J, Kaminsky J. Overlying breast as a cause of false-positive thallium scans. *Clin Nucl Med* 1978;3:229.
- Garver PR, Wasnich RD, Shibuya AM, Yeh F. Appearance of breast attenuation artifacts with thallium myocardial SPECT imaging. *Clin Nucl Med* 1985;10:694–696.
- Fleming JS. A technique for using CT images in attenuation correction and quantification in SPECT. *Nucl Med Commun* 1989;10:83–97.
- Madsen MT, Kirchner PT, Edlin J, Nathan M, Kahn D. An emission based technique for obtaining attenuation correction data for myocardial SPECT studies. *Nucl Med Commun* 1993;14:689–695.
- Younes RB, Mas M, Bidet R. A fully automated contour detection algorithm: the preliminary step for scatter and attenuation compensation in SPECT. *Eur J Nucl Med* 1988;14:586–589.
- Hosoba M, Wani H, Toyama H, Murata H, Tanaka E. Automated body contour detection in SPECT: effects on quantitative studies. *J Nucl Med* 1986;27:1184–1191.
- Gullberg GT, Malko JA, Eisner RL. Boundary determination methods of attenuation correction in SPECT. In: Esser PD, ed. *Emission computed tomography: current trends*. NY: Society of Nuclear Medicine; 1983:33–53.
- Galt JR, Cullom SJ, Garcia EV. SPECT quantification: a simplified method of attenuation and scatter correction for cardiac imaging. *J Nucl Med* 1992;33:2232–2237.
- Meikle SR, Dahlbom M, Cherry SR. Attenuation correction using count-limited transmission data in positron emission tomography. *J Nucl Med* 1993;34:143–150.
- Xu EZ, Mullani NA, Gould KL, Anderson WL. A segmented attenuation correction for PET. *J Nucl Med* 1991;32:161–165.
- Lange K, Carson R. EM reconstruction algorithms for emission and transmission tomography. *J Comp Assist Tomogr* 1984;8:306–316.
- Miller MI, Snyder DL, Miller TR. Maximum-likelihood reconstruction for single-photon emission computed tomography. *IEEE Trans Nucl Sci* 1985; NS-32:769–778.
- Wallis JW, Miller TR. Rapidly converging iterative reconstruction algorithms in single-photon emission computed tomography. *J Nucl Med* 1993; 34:1793–1800.
- Chornoboy ES, Chen CJ, Miller MI, Miller TR, Snyder DL. An evaluation of maximum likelihood reconstruction for SPECT. *IEEE Trans Med Imaging* 1990;9:99–110.
- Zeng GL, Gullberg GT, Tsui BMW, Terry JA. Three-dimensional iterative reconstruction algorithms with attenuation and geometric point response corrections. *IEEE Trans Nucl Sci* 1991;38:693–702.
- Penney BC, King MA. A projector, back-projector pair which accounts for the two-dimensional depth and distance dependent blurring in SPECT. *IEEE Trans Nucl Sci* 1990;37:681–686.
- Liang Z, Turkington TG, Gilland DR, Jaszczak RJ, Coleman RE. Simultaneous compensation for attenuation, scatter and detector response for SPECT reconstruction in three dimensions. *Phys Med Biol* 1992;37:587–603.